Multiscale investigation of bonded granular materials: The H-bond model

Zeyong Liu, Francois Nicot, Antoine Wautier, Felix Darve

Multiscale investigation of bonded granular materials: the *H*-bond model

Zeyong Liu [a], Francois Nicot [a], Antoine Wautier [b], Felix Darve [c]

[a] *Université Savoie Mont-Blanc, ISTerre, Le Bourget-du-Lac, France*
[b] *Aix-Marseille University, INRAE, RECOVER, Aix-en-Provence, France*
[c] *Université Grenoble-Alpes, Laboratoire Sols Solides Structures, Grenoble, France*

Abstract

Cemented granular materials play an important role in both natural and engineered structures, as they are able to resist traction forces. However, modeling the mechanical behavior of such materials is still challenging, and most of existing constitutive models follow phenomenological approaches that unavoidably disregard the microstructural mechanisms taking place on the bonded grains scale. This paper presents a multiscale approach applicable to any kind of granular materials with solid bonds between particles. Inspired from the *H*-model, this approach allows simulating the behavior of cemented materials along various loading paths, by describing the elementary mechanisms taking place between bonded grains. In particular, the effect of local bond failure process on the macroscopic response of the whole specimen is investigated according to the bond strength characteristics.

Key words: Cemented granular materials, bonded contact model, H-model, meso-structure, multiscale approach, homogenization

1. Introduction

Cohesive geomaterials are widespread in a variety of engineering purposes (such as natural and artificial cemented sands, concrete, and sedimentary rocks), where solid bonding is known as an important characteristic (Pettijohn et al., 1987; Leroueil and Vaughan, 1990; Cuccovillo and Coop, 1999). The solid bonding includes i) natural cementation originating from various processes and infill materials such as oxidative precipitates or clays (Cuccovillo and Coop, 1997; Ismail et al., 2002; Yin and Karstunen, 2011; Lin et al., 2016) and ii) artificial cementation where soil can be mixed with cement, lime, bacteria producing calcite or other adhesive materials (Lade and Overton, 1989; Huang and Airey, 1998; Gao and Zhao, 2012; Rios et al., 2014; Montoya and DeJong, 2015; Terzis and Laloui, 2018; Nafisi et al., 2019; Xiao et al., 2021). Through the influence of solid bonds, these cemented geomaterials typically exhibit distinctive behaviors in comparison to their unbonded counterparts, and it has been recognized that they play an important role in engineering (Leroueil and Vaughan, 1990; Kochmanová and Tanaka, 2011; Rahman et al., 2010). Hence, solid bonds should be taken into account to better understand the mechanical behavior of cemented geomaterials.

Historically, experiments that capture the mechanical behavior of solid bonds have shown that many peculiar features distinguish cemented geomaterials from non-cemented ones such as a substantial softening for stress–strain response, a slight increase in residual friction at critical state (Rahman et al., 2018) and a more dilative volumetric response (Abdulla and Kiousis, 1997; Tang et al., 2007; Feng et al., 2017). This was put forward for both natural (Burland, 1990; Rouainia and Muir wood, 2000; Rocchi et al., 2003) or artificial cemented specimens (Coop and Atkinson, 1994; Consoli et al., 2007; Gao and Zhao, 2012), which motivated the development of several constitutive models for cemented geomaterials (Rotta et al., 2003; Rabbi et al., 2011; Jiang et al., 2013).

As it remains challenging to observe and quantify the failure of cementation at microscale, a global phenomenological approach is often used in constitutive modeling (Rouainia and Muir wood, 2000; Taheri et al., 2012). However, such models fail in properly accounting for the underpinning microscopic mechanisms. As an alternative, the discrete element method (DEM) emerges as a potent tool for enhancing the comprehension of the link between local bond breakage and global, constitutive characteristics in cemented geomaterials (Jiang et al., 2014a; Wu et al., 2021). This is attributed to its capability to relate macroscopic responses to microscopic information, such as bond breakage (Wang and Leung, 2008).

To feed DEM approaches, many previous studies have so far focused on bonded contact models between grains (Obermayr et al., 2013; Jiang et al., 2014a; Shen et al., 2016; Zhang and Dieudonné, 2023). For existing bonded contact models, the bond geometry between two grains is simplified, usually idealizing a bond as a short beam connecting the surfaces of two adjoining grains (Jiang et al., 2014b; Brendel et al., 2011; Yang et al., 2019). Such a microstructure where two particles and a bond are linked together can be referred to as a triad.

Previous researchers have developed several continuum constitutive models to describe some important features of cemented granular materials (Kavvadas and Amorosi, 2000; Rocchi et al., 2003; Evans et al., 2014; Li et al., 2017; Khoubani, 2018). Multiscale approaches can be used to describe the bond behavior on the grain scale via specific bonded contact laws. Thanks to homogenization techniques, the macroscopic constitutive properties emerge from the collective response of the microstructural bodies (Mehrabadi et al., 1997; Balendran and Nemat-Nasser, 1993a and 1993b; Nemat-Nasser, 2000; Nemat-Nasser and Zhang, 2002). The micro-directional model (Nicot and Darve, 2005) stands as an example of micromechanically-based model, where the granular assembly can be described as a collection of contacts between pairs of adjoining spherical grains with different orientations in the physical space. In order to enrich the microstructural description, this model was extended to the H-model (Nicot and Darve, 2011a and 2011b; Xiong et al., 2017; Xiong et al., 2021) by including an intermediate scale. The 2D H-model was derived from hexagonal mesostructures composed of six monodisperse, spherical grains in contact, forming a closed hexagonal loop. The H-model was shown to be a very potent micromechanical model in order to capture most of the salient constitutive features of granular materials (Wautier et al., 2021).

This paper aims to investigate the influence of solid bonds on the response of granular assemblies, by accounting for underpinning microstructural mechanisms. For this purpose, the 2D *H*-model is considered and extended by including solid bonds between the grains in contact. The response of different specimens is then analyzed along classical loading paths (i.e. biaxial loading path, and proportional strain loading path). Several key aspects are investigated, such as bonded and unbonded global behavior, bond failure mechanisms along the different loading paths. The results are eventually discussed in terms of the macroscopic responses in relation to micromechanical aspects, including detailed analyses on the influences of the bond breakage.

Time differential of any variable ψ will be denoted $\delta\psi$, as the product of the particulate derivative $\dot{\psi}$ by the infinitesimal time increment δt.

2. *H*-model and physical mechanisms of bonded materials

2.1 *H*-model in brief

The general principle of the *H*-model consists in a statistical description of the microstructure of granular assemblies. A homogenization process is developed by averaging the local behavior taking place at the intermediate scale corresponding to hexagonal sets of grains.

Basically, the elementary unit for the 2D original *H*-model is a hexagonal pattern (denoted H-cell) composed of six spherical particles with the same radius interacting through contact laws. Each cell is assumed to be loaded by a symmetric set of forces, as illustrated in Fig. 1.

Compared with the original H-model that accounts for elasto-frictional behavior at contacts, a cemented assembly can be described by updating the contact law. Bond 1 acts on the contact between particle 1 and particle 2, where both normal and tangential contact forces are present. Bond 2 acts on the contact between particle 2 and particle 3, where only a normal contact force is involved because of the symmetry preservation, as shown in Fig. 1. In the H-model, grains are assumed not to rotate. This is imposed through additional external forces G_2 that ensure the momentum balance for all grains.

The testing procedure will be described in detail in section 3, where some classical loading paths involving traction, compression, and shear mechanisms are considered.

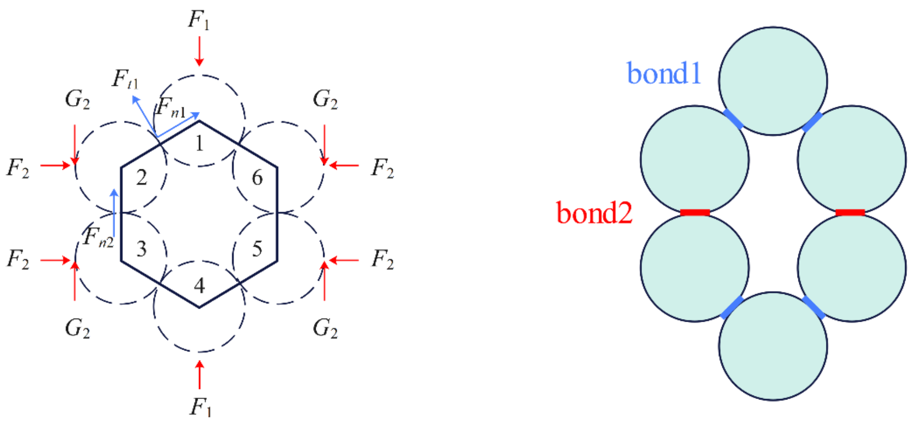

Fig. 1. Description of forces and bonds in a given hexagonal meso-structure.

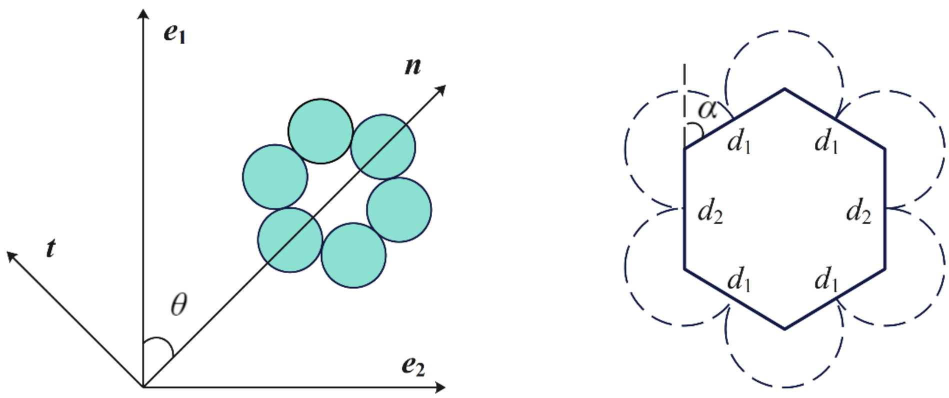

Fig. 2. Global coordinates ($\boldsymbol{e}_1$, $\boldsymbol{e}_2$) and mesoscale coordinates ($\boldsymbol{n}$, $\boldsymbol{t}$) (left); geometrical settings (right).

2.2 Bonded contact model

Bonded contact models can be presented in the general framework of bonded granular materials (Ismail et al., 2002; Jiang et al., 2014b). The material constituting the bonds between particle can be regarded as a brittle elastic medium. The bonded contact model between grains considers that the two grains and the bond (elementary triad) are deformable. In the elastic regime, as seen in Fig. 3, a triad can be described by three springs mounted in series, both along normal and tangential directions.

The contact forces acting at inter-particle contacts (normal contact force F_n and tangential contact force F_t) can be related to the relative displacements (normal component u_n and tangential component u_t) as follows in the elastic regime:

$$\delta F_n = k_n \delta u_n \tag{1}$$

$$\delta F_t = k_t \delta u_t \tag{2}$$

For a serial bonded contact model, the bond material acts as an additional spring in series. The stiffness of the spring triad (Fig. 3) is denoted as k_n and k_t for normal direction, and tangential direction, respectively. In a serial assembly, the contact stiffness is controlled by the particle stiffness and bond stiffness as follows:

$$k_n = \frac{k_{np} k_{nb}}{2k_{nb} + k_{np}} \tag{3}$$

$$k_t = \frac{k_{tp} k_{tb}}{2k_{tb} + k_{tp}} \tag{4}$$

where k_{np} and k_{tp} refer to particle stiffness in normal and tangential directions, whereas k_{nb} and k_{tb} refer to bond material stiffness in normal and tangential directions.

In this manuscript, once the strength limit of the bond is reached, the bond fails and is considered not to exist any longer. Fig. 4 presents the unbonded contact model after bond failure, in which only two particles contact. In the normal direction, an elastic behavior is considered, and only a compressive force can be transmitted. In the tangential direction, an elasto-frictional law is activated. Details of the classical contact law for the original *H*-model can be found in (Nicot and Darve, 2011b). The residual contact law is expressed as follows:

$$\delta F_n = k'_n \delta u_n \tag{5}$$

$$\delta F_t = \begin{cases} k'_t \delta u_t & \text{elastic regime} \\ \tan\varphi_g (F_n + k'_n \delta u_n) - F_t & \text{plastic regime} \end{cases} \tag{6}$$

For the unbonded contact model, the deformability of particles is modeled through the overlap due to the relative displacement of the two particles. Compared with the bonded contact, once the bond has failed, both normal and tangential stiffnesses of a bond are supposed to be infinite ($k_{nb} = \infty$, $k_{tb} = \infty$). Thus, the contact stiffness can simply be obtained from equations (3) and (4), and reads:

$$k'_n = \frac{k_{np}}{2} \tag{7}$$

$$k_t' = \frac{k_{tp}}{2} \tag{8}$$

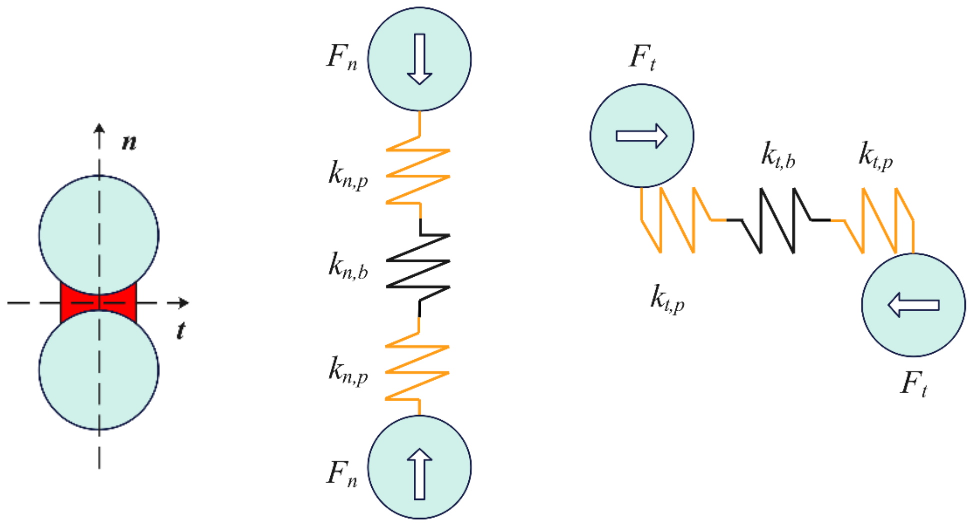

Fig. 3. Serial bonded contact model with mechanical components (orange: mechanical spring for particles; black: mechanical spring for bond material).

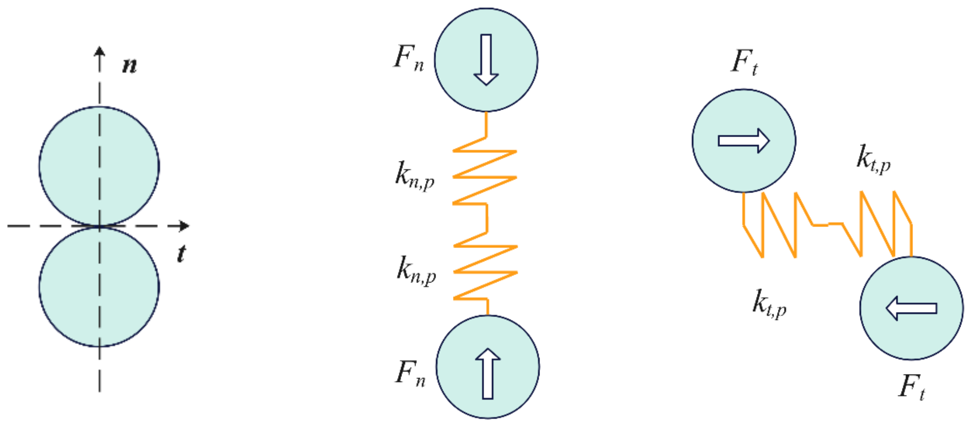

Fig. 4. Details of the unbonded contact model in the elastic regime.

2.3 Bond failure criterion

In order to simplify the constitutive model, it is assumed that a bond between particles breaks abruptly according to a brittle failure type. The bond failure criterion includes three basic modes (compression, traction, and shear), as shown in Fig. 5. Compression failure occurs when the normal contact force exceeds the compressive bond strength. Traction failure occurs when a bond is under traction with a normal contact force reaching the traction bond strength. The limit of normal contact forces can be expressed as:

$$F_n = \begin{cases} R_{n,c} & \text{compression} \\ R_{n,t} & \text{traction} \end{cases} \tag{9}$$

where $R_{n,c}$ is the compressive bond strength; $R_{n,t}$ is the traction bond strength.

Furthermore, shear failure occurs once the tangential contact force reaches the shear bond strength R_s:

$$F_t = R_s \tag{10}$$

Finally, as shown in Fig. 5, three failure mechanisms coexist for bonded contacts. The sign of the normal contact force determines the mechanical regime (compression regime or traction regime, with compressive forces counted positive):

$$\begin{cases} R_{n,c} > F_n > 0 & \text{compression} \\ R_{n,t} < F_n < 0 & \text{traction} \\ |F_t| > R_s & \text{shear} \end{cases} \tag{11}$$

The resulting contact after bond breakage behaves as an unbonded contact. It means that the bond material at a serial bonded contact admits an infinite stiffness at the instant of bond failure. The system immediately transforms into particle-to-particle contact, and the contact forces will evolve along the loading path with the contact law given in equations (5) – (6).

The existence of a bond gives rise to a variation in the contact force when failure occurs. Fig. 6 shows the evolution of the normal contact force with the normal displacement. In compression regime, the normal contact force varies linearly with the normal displacement. After bond failure in a compression regime, the contact between the particles still exists as a particle-to-particle contact. In this case, the change in contact stiffness causes the normal contact force to evolve with another slope. In Fig. 6, it can be seen that a zero force with a non-zero overlapping will be obtained if an unloading is performed after bond failure. This is consistent with the damage mechanics framework (Mazars and Pijaudier-Cabot, 1989; Giry et al., 2011), inducing a change in stiffness directed by the vanishing of the broken bond. Further details can be found in appendix A. In traction regime, the normal contact force increases while the bond exists and drops to zero at the moment of bond failure. The existence of contacts between particles for each H-cell after bond failure is checked from the geometrical parameters of the H-cell. The contact 1 is lost when $d_1 > 2r$, and the contact 2 is lost when $d_2 > 2r$, as shown in Fig. 2. If no contacts exist anymore, the meso-stress for such an H-cell drops down to 0.

As for the tangential contact force, an elastic response exists before bond failure occurs. After failure, the contact model transforms into an elasto-frictional model. Finally, as shown in Fig. 7a, the evolution of contact forces can be represented in the plane of normal and tangential forces, where a bond strength box gives the limit of these components. Four typical failure situations can be identified, as depicted in Fig. 7b with the four colored lines. It can be seen that when the bond fails in a traction regime, the contact forces drop to zero once the bond is broken. When the bond fails in a compression regime, the contact is described by an elasto-frictional contact law, with a change in the slope of the normal contact force, as seen in Fig. 7b.

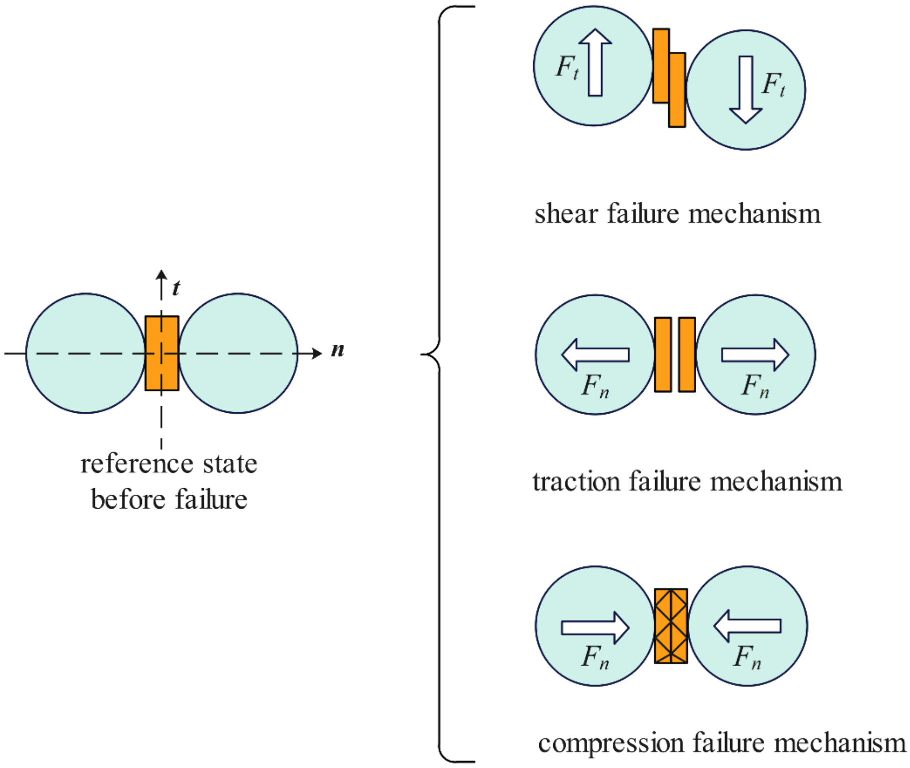

Fig. 5. Three modes of bond failure for the bonded contact model.

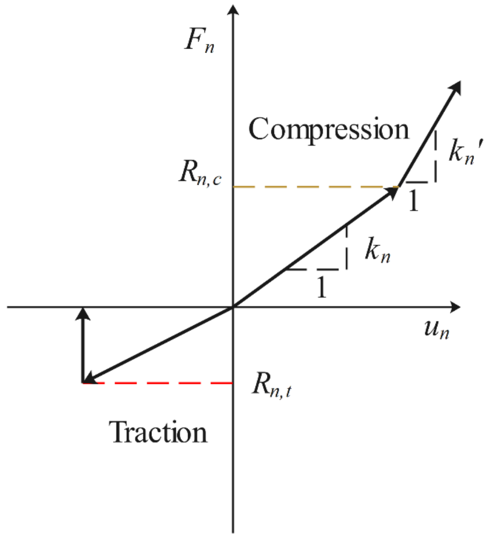

Fig. 6. Mechanical model along the normal contact direction.

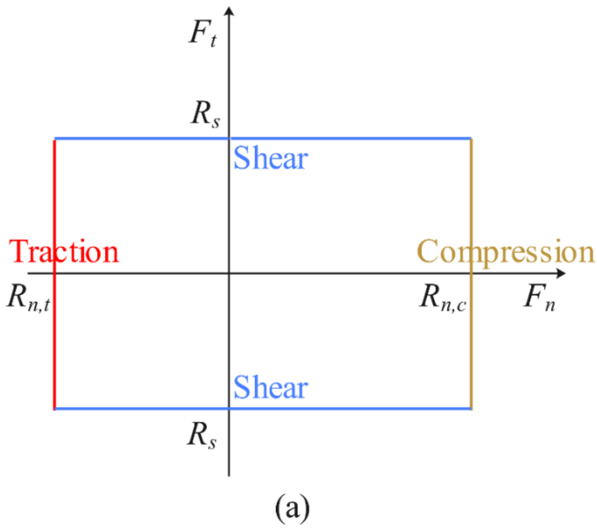

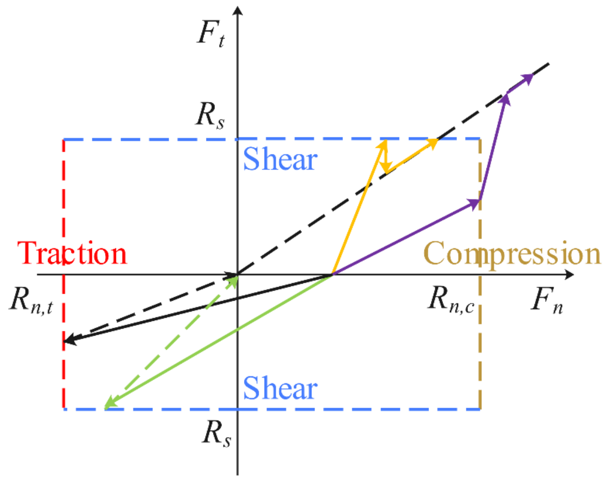

(b)

Fig. 7. Failure surface (a) and mechanical behavior of a triad (b) in the contact forces (F_n and F_t) plane.

3. Numerical inspection of the *H*-bond model capability

The original *H*-model is able to account for geometric changes in the microstructure of granular materials through the deformation of elementary hexagonal patterns at mesoscale. This feature makes the *H*-model able to capture most of the salient constitutive features of granular assemblies, as observed along classical loading paths (Nicot and Darve, 2011b).

In this section, the capability of the *H*-bond model, equipped with the bonded contact model detailed in the previous section, is analyzed.

3.1 Typical mechanical response of cemented materials

Figure 8 presents some typical results extracted from the literature, corresponding to deviatoric stress responses during experimental biaxial loading tests with artificially cemented sands (Wang and Leung, 2008), together with the numerical response for the same materials during DEM simulations (Jiang et al., 2013). The cement content of the experimental specimen was determined from the weight ratio, i.e. the weight of the cement to the total dry weight of the soil-cement mixture. The bonded loose specimens used during the DEM simulations were prepared homogenously, which required identical bonds to be formed at each contact. It can be noted that the simulated deviatoric stress curves have the same trend as those obtained experimentally. A softening behavior can be observed for cemented samples after a stress peak is reached, while the uncemented specimens experience a monotonous hardening regime. Fig. 8 also shows that the increasing bond strength contributes to an increase in the peak stress.

In the next section, the ability of the *H*-bond model to reproduce these features is explored.

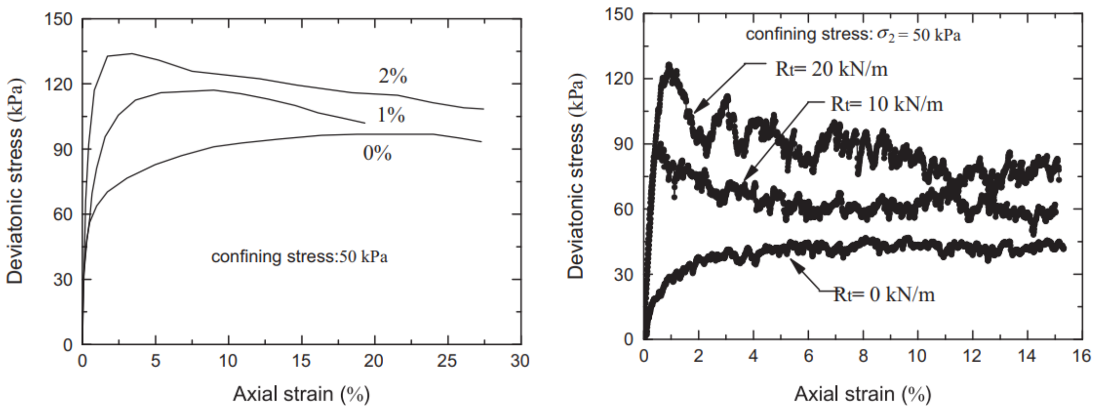

Fig. 8. Stress–strain responses of granular specimens: (a) experimental data (Wang and Leung, 2008); (b) DEM results (Jiang et al., 2013).

3.2 Numerical simulations of cemented materials using the *H*-bond model

An isotropic statistical distribution of H-cells is used throughout this section.
The general scheme of the *H*-bond-model is summarized as follows:

1. The strain homogeneity hypothesis allows to update the H-cell geometry in accordance with the macroscopic strain increments.
2. The relative deformations at contact scale for each H-cell are computed to fulfill static equilibrium.
3. The contact forces are updated based on the incremental evolution of the H-cell geometry.
4. The macroscopic stresses are ultimately derived by statistical averaging of all meso-stresses acting within each H-cell.

The numerical parameters used to run the simulation are reported in Table 1. It is worth noting that bonds and particles are supposed to be made up of the same material. The micromechanical parameters are therefore the same for bonds and particles. In the simulations, an isotropic consolidation is first imposed until a confining pressure of 100 kPa is reached. Then, the sample undergoes a given loading path by imposing a strain loading in the axial direction, while specific lateral loading conditions are prescribed.

Table 1
Summary of parameters used for the *H*-bond model simulation.

Parameter	Symbol	Unit	Value
Normal contact stiffness of particles	k_{np}	N/m	$4*10^8$
Normal contact stiffness of bond	k_{nb}	N/m	$4*10^8$
Contact stiffness ratio	$\frac{k_t}{k_n}$	-	0.5
Compressive bond strength	$R_{n,c}$	kN	500

Tractive bond strength	$R_{n,t}$	kN	500
Shear bond strength	R_s	kN	900
Inter-granular friction angle	φ_g	deg	30
Initial opening angle	α_0	deg	40
Number of directions	N_θ	-	360

Biaxial loading and proportional strain loading paths are considered in order to combine compression, traction and shear failure regimes at the mesoscopic scale. This allows to mix different bond failure modes along the mechanical response of the specimens, and analyze how they interact with each other.

A biaxial test is first simulated under a constant lateral stress, while a constant strain rate is imposed in the axial direction: both $\dot{\varepsilon}_1$ and σ_2 are constant. Proportional strain loading paths are also considered. For such loading paths, the imposed axial strain rate is constant while the lateral stain rate is proportional to the axial strain rate: $\dot{\varepsilon}_2 = \lambda\dot{\varepsilon}_1$. As the incremental volumetric strain is given by $\dot{\varepsilon}_v = (1+\lambda)\dot{\varepsilon}_1$, three regimes can be explored:

$$\begin{cases} \lambda > -1 & \text{contractant regime} \\ \lambda = -1 & \text{isochoric regime} \\ \lambda < -1 & \text{dilatant regime} \end{cases} \tag{12}$$

3.2.1 Biaxial loading path

The macroscopic stress and strain responses are explored in 2D conditions by considering the mean stress $p = (\sigma_1 + \sigma_2)/2$, the deviatoric stress $q = \sigma_2 - \sigma_1$, and the volumetric strain $\varepsilon_v = \varepsilon_1 + \varepsilon_2$, where σ_1 and σ_2 are the principal stresses, and ε_1 and ε_2 are the principal strains oriented along axial (1) and lateral (2) directions.

A dense sample is considered, either with bonded particles, or with unbonded particles. The unbonded specimen is considered as a reference. The typical macroscopic responses obtained are reported in Fig. 9.

The stress–strain responses of the cemented specimen differ from the response of the unbonded specimen. It can be observed that the bond effect is dominant in the early stage of loading, where a higher stress peak occurs for the cemented specimen, followed by a more pronounced softening behavior. Likewise, larger contractancy develops at small strains for the cemented specimen.

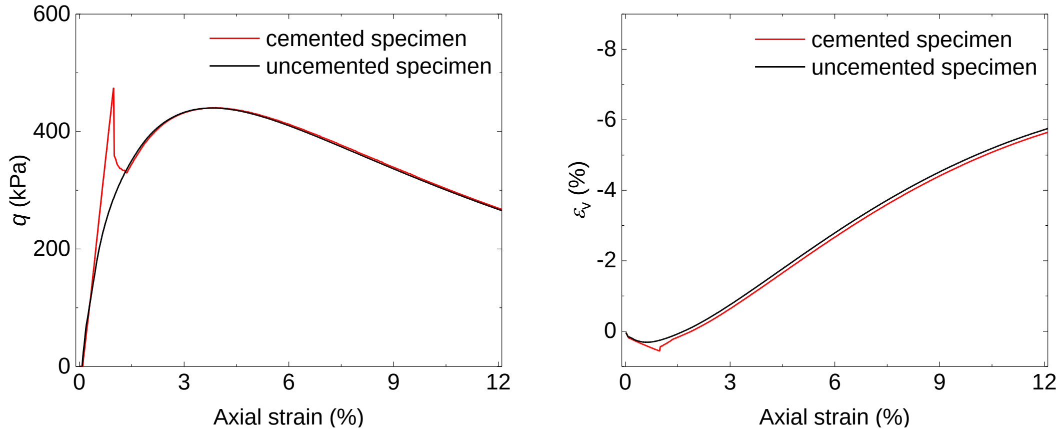

Fig. 9. Deviatoric stress and volumetric strain responses along the biaxial loading; cemented and uncemented specimens.

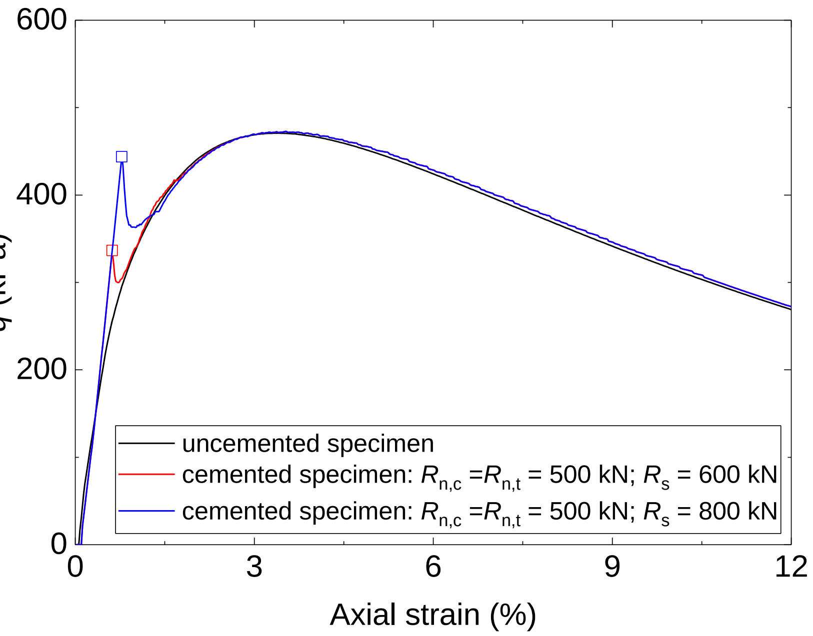

(a)

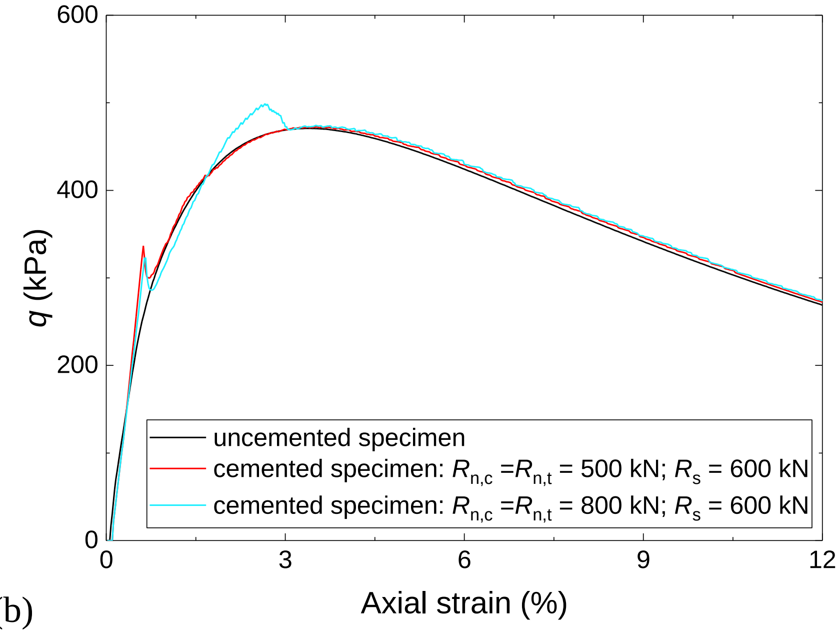

(b)

Fig. 10. Deviatoric stress along the biaxial test with different bond strengths; (a) different shear strengths, and (b) different compression/traction strengths.

It can also be observed in Fig. 9 that the deviatoric stress curve exhibits two peaks. The first stress peak stems from an intense bond failure activity, occurring along specific orientations of the H-cells. For these cells, the bonded contacts transform into cohesionless contacts. Among them, some H-cells were in traction regime at failure, which results in a contact opening with subsequent macroscopic stress decrease. Ultimately, when most of the bonds have broken, the specimen evolves as the unbonded specimen: a second stress peak is reached, followed by a softening regime.

The influence of the bond strength (in traction, compression, or shear) is explored in Fig. 10. For this purpose, different values of bond strength are considered. The first case corresponds to different shear strengths ($R_{n,c} = R_{n,t} =$ 500 kN; $R_s =$ 600 kN, 800 kN), as shown in Fig. 10a. It can be observed that the increase in shear strength leads to an increase in the first peak stress. The failure of bond in shear occurs first, and affects the response of bond failure in traction due to the change of stiffness. The increase in shear strength delays the bond failure in shear, and likewise delays the bond failure in traction, which results in an increase in the first peak stress. Fig. 10b shows the effects of different traction and compression strengths ($R_{n,c} = R_{n,t} =$ 500 kN, 800kN; $R_s =$ 600 kN). The traction and compression strengths mainly affect the loading sequence during which the failure in traction occurs successively within the bonds belonging to different cell orientations. Thus, the increase in the traction strength makes the bonded specimen convert into an unbonded specimen ($R_{n,c} = R_{n,t} =$ 800kN; $R_s =$ 600 kN), as shown in Fig. 10b.

3.2.2 Proportional strain loading path

The evolution of the deviatoric stress as a function of the axial strain is given in Fig. 11. Contractant, isochoric, and dilatant proportional strain loading paths are considered with $\lambda = -0.8, -1, -1.2$, respectively. For the contractant case ($\lambda =$ -0.8), it can be observed that the deviatoric stress increases continuously. When $\lambda = -1$, zero volume change is imposed, and the deviatoric stress increases until it reaches a plateau. When $\lambda = -1.2$, the deviatoric stress increases at first and then decreases gradually after the peak, corresponding to a static liquefaction process where most of the bonded contacts open.

The bond failure evolution is given in Fig. 12. It can be observed that the bonds fail in compression regime first, whatever the volumetric strain regime (contractant, dilatant or isochoric). This is due to the fact that at the beginning of the loading, the bonds with the largest stress are in a compressive regime. This is all the more noticeable when the volumetric strain regime is contractant. Then, the contacts behaving in a traction regime fail once the tensile strength is reached. It should be noted that this bond failure evolution depends on the relative bond strengths in compression, tension and shear. For example, much larger values in compression strengths could lead to a different scenario by limiting the bond failure in compression.

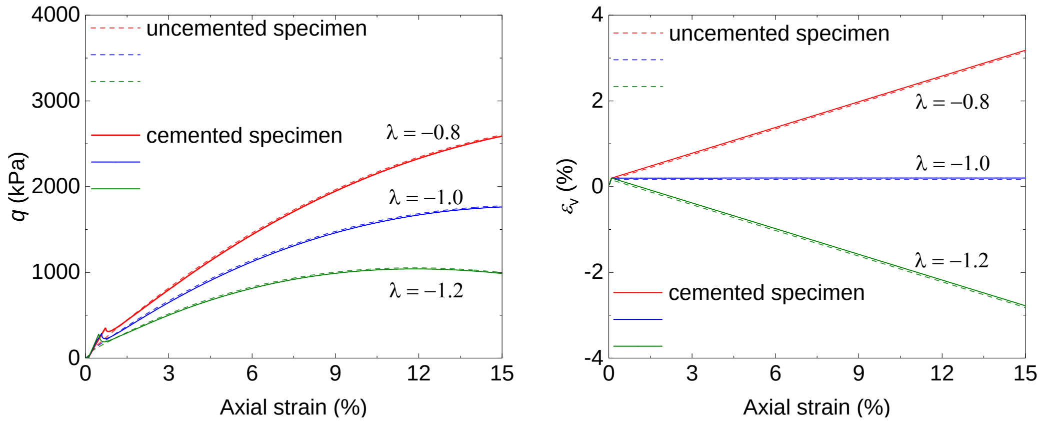

Fig. 11. Macroscopic response of a cemented specimen along proportional strain loading paths.

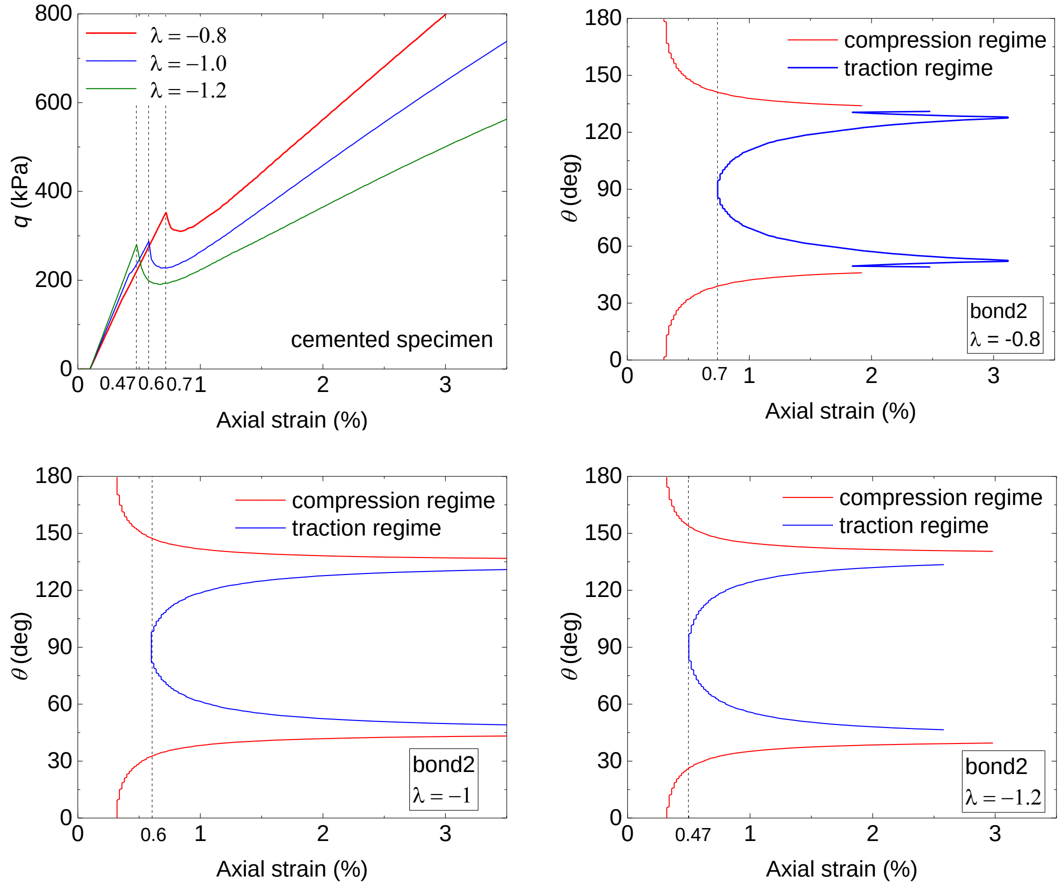

Fig. 12. Map of bond failure (bond 2) along the three proportional strain loading paths in terms of H-cells distribution. For each H-cell orientation (Θ), the axial strain at which bond 2 fails is given. Failure in compression appears in red while failure in traction appears in blue. The vertical dotted line highlights the axial strain at which bonds start failing in traction.

3.3 Quantitative analysis of bond failure

In order to track the process of bond failure during the loading path, the concepts of bond failure ratio and bond failure rate are introduced. The bond failure ratio is defined as the number of broken bonds over the total number of bonds, and can be expressed as:

$$R_i = \frac{n_b}{N_b} \tag{13}$$

where N_b is the total number of bonds at the initial state, and n_b is the cumulated number of broken bonds at a given axial strain ε_1. With six bonded contacts per H-cell, N_b is equal to six times the number of H-cells.

The bond failure rate is then defined as the bond failure ratio increment over a given (constant) axial strain increment, and can be expressed as:

$$r_i = \frac{dR_i}{d\varepsilon_1} \tag{14}$$

where dR_i is the bond failure ratio increment observed over the axial strain increment $d\varepsilon_1$.

Figure 13 focuses on the evolution of the bond failure rate with respect to the axial strain in the beginning of the biaxial loading. It reveals that the peak of the bond failure rate coincides with the peak stress, and is followed by a sharp, subsequent decrease. The evolution of the bond failure ratio along the loading path is given in Fig. 14. The figure shows that the bond failure ratio increases with two different regimes. The A-B stage corresponds to a compressive bond failure regime, whereas the B-D stage corresponds to a shear and a traction bond failure regime.

Two peaks are observed (Fig. 13b). The first peak (point A) corresponds to the bonds undergoing a compressive failure. As a consequence, this first peak has no important effect on the stress-strain response curve of the specimen. The second peak is observed at point B, which nearly corresponds to the peak stress of the deviatoric stress curve. At this stage, the tensile failure of bonds takes place massively, as shown in Fig. 14b. As the bonds break in traction, contacts open, and the corresponding H-cells vanish, resulting in fewer H-cells contributing to the macroscopic stress. Hence, a remarkable reduction in the macroscopic stress occurs, leading to a noticeable softening.

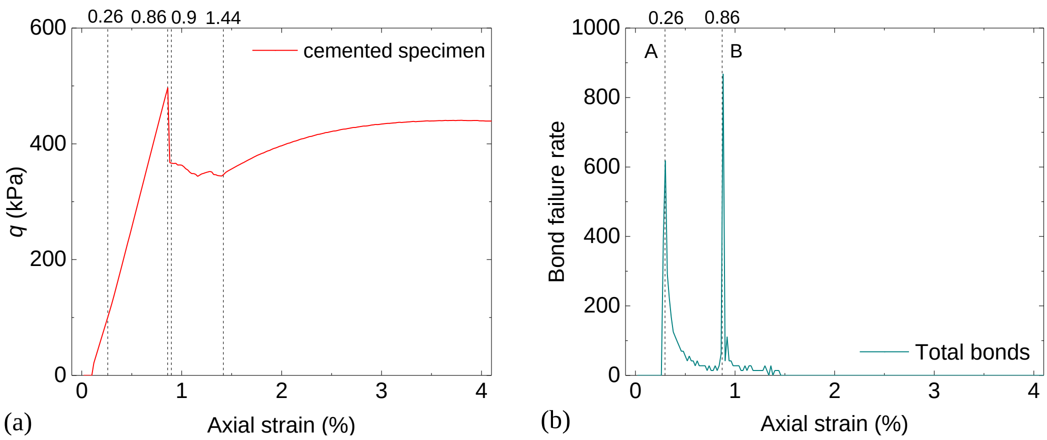

Fig. 13. Deviatoric stress evolution along a biaxial loading path, with the axial strain up to 4% (a), and corresponding evolution of bond failure rate (b).

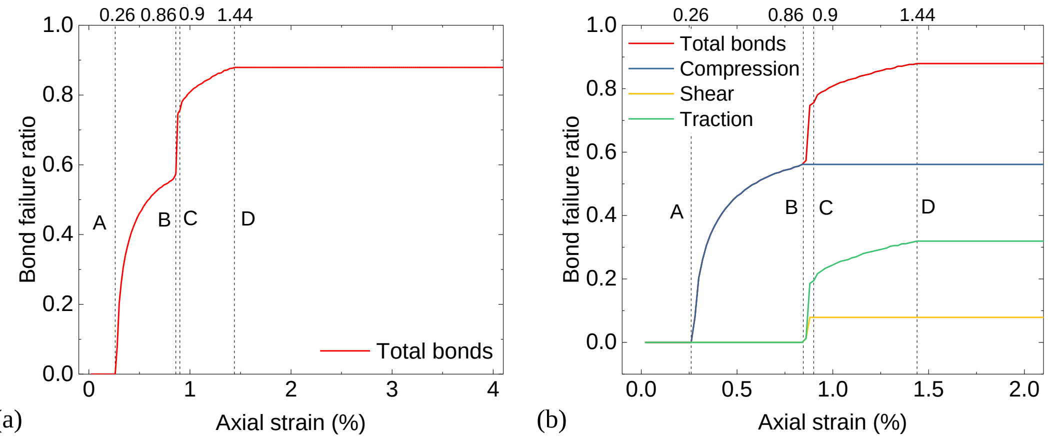

Fig. 14. Evolution of the bond failure ratio with the axial strain (a), and corresponding bond failure modes (b).

3.4 Micro-mechanical analysis of failure in cemented materials

In order to better understand how the bond failure evolution affects the macroscopic response of a given cemented specimen, the microscopic mechanical responses obtained from the *H*-bond model on the H-cell scale, such as contact forces or mesoscopic strains, are investigated in this section.

Fig. **15** shows that the volumetric strain of the cemented specimen gives rise to a strong contractancy followed with a quick volume change at the axial state (0.86%) due to massive bond failure in traction regime (Fig. 14b). The lateral strain ε_2 of the cemented specimen is first in compression and then gradually evolves into extension with the purpose of keeping σ_2 constant, which leads to a transition along some H-cell directions from a compression regime to a traction regime. Bond failure in traction regime also has a noticeable effect at the axial state ε_2 =0.86%. The subsequent contact opening results in a sharp increase in the lateral strain of the cemented specimen, as shown in Fig. 15b.

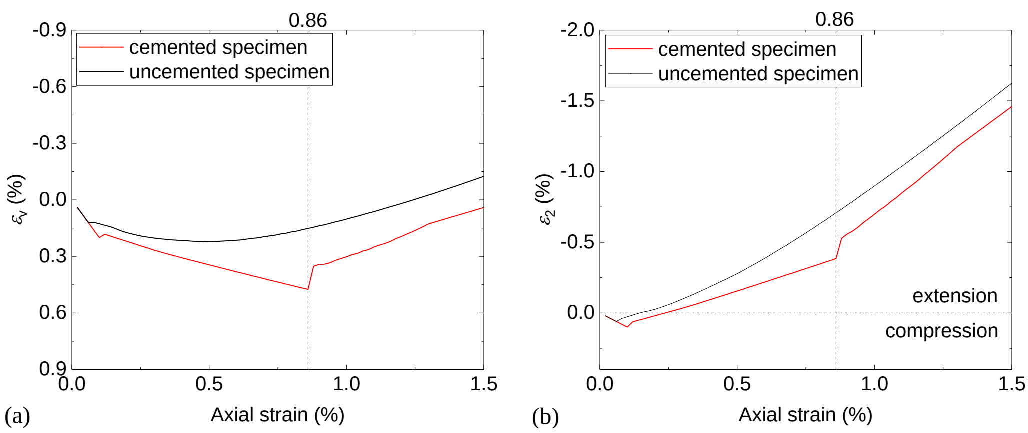

Fig. 15. Volumetric strain responses (a) and lateral strain responses (b) along the biaxial loading for

cemented and uncemented specimens.

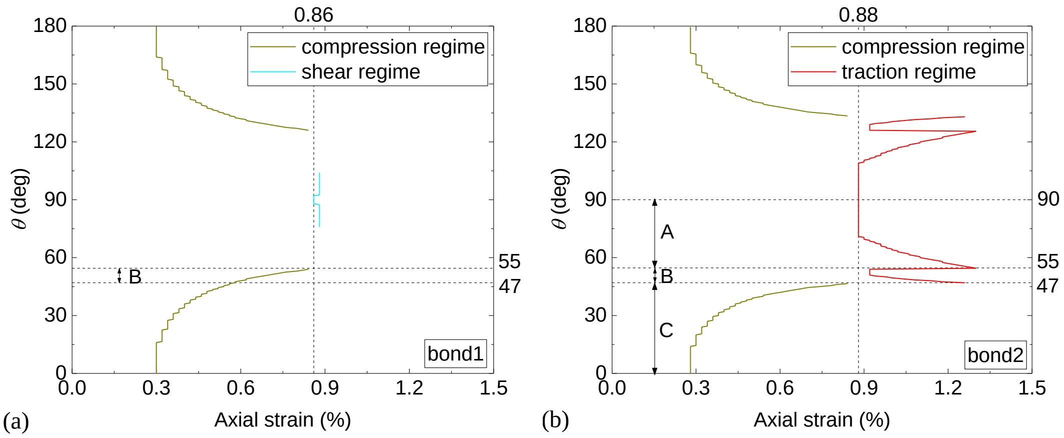

Fig. 16. Maps of bond failure occurrence along a biaxial loading path. For each H-cell orientation (Θ), the axial strain at which bond 1 fails is given. Failure in compression appears in dark green, failure in shear appears in light blue and failure in traction appears in red. The vertical dotted lines highlight the axial strain at which bonds start failing in shear and in traction.

Fig. **16** presents the bond failure evolution with respect to the axial strain. Whatever the bond category (bond 1 or bond 2), the bonds break in compression regime first in the early stage of the loading. Then, the bonds 2 break in a traction regime. This is due to the fact that H-cells orientations are distributed in the range from 0 deg to 180 deg ($\theta = 0$ deg corresponds to H-cell aligned with the axial direction, while $\theta = 90$ deg to H-cells aligned with the lateral direction). In terms of H-cell orientations, three domains (A, B, and C) are illustrated with respect to different regimes of bond failure, as shown in Fig. 16b. In the domain A, the response of H-cells is dominated by the failure of bond 1 in shear and the failure of bond 2 in traction. In the domain C, both bond 1 and bond 2 experience failure in a compression regime. In the domain B, the failure of bond 1 in compression influences the behavior of bond 2 due to the change in contact stiffness (k_n and k_t), making bond 2 brake earlier in a traction regime.

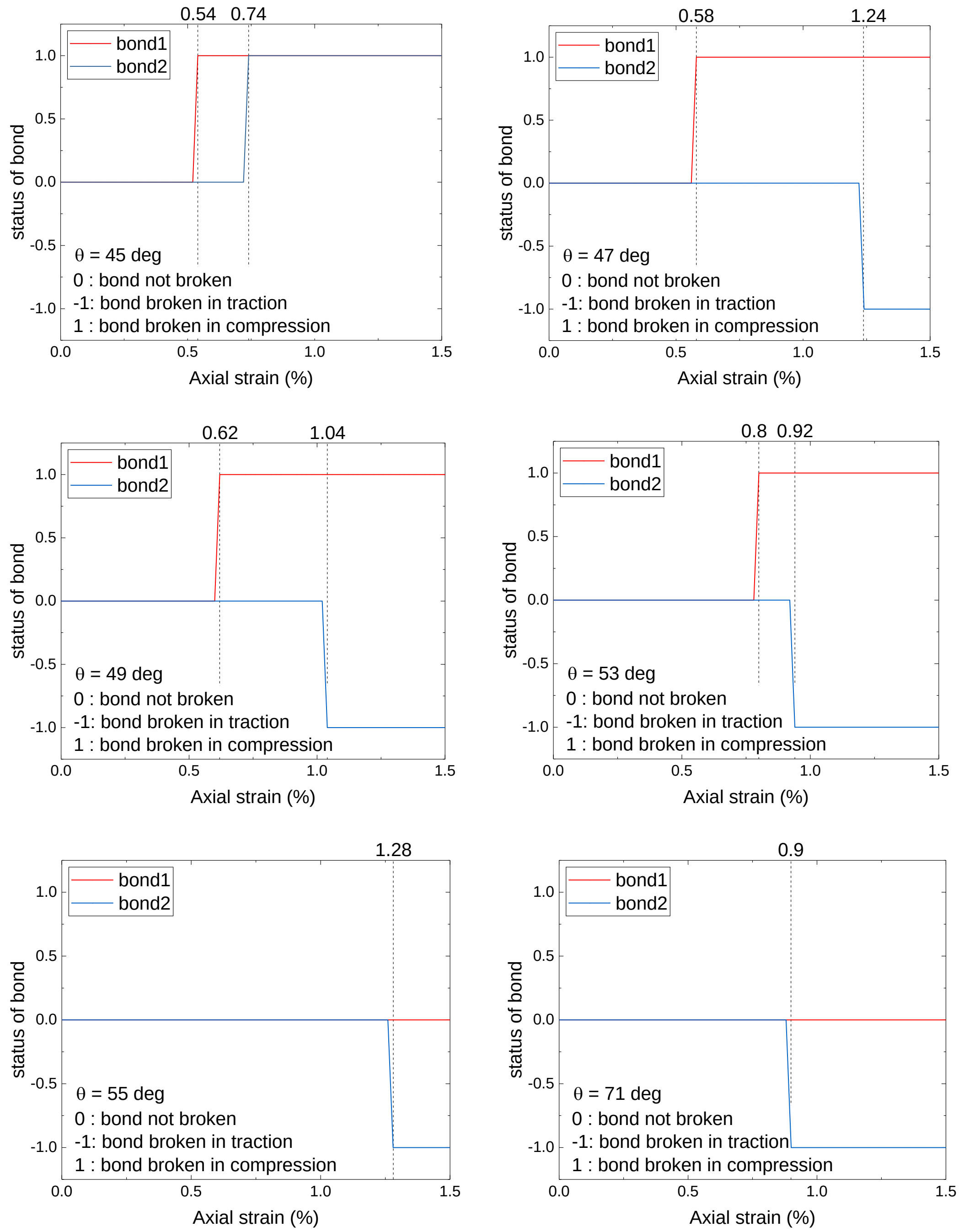

Fig. 17. Status of bond 1 and bond 2 in a H-cell along a biaxial loading path, in terms of the H-cell orientation (45 deg, 47 deg, 49 deg, 53 deg, 55 deg, 71 deg).

Figure 17 depicts the bond failure chronology for a H-cell oriented in a certain direction along the loading path. The response of the H-cell in the direction (45 deg) is marked by the failure of bonds in compression as shown in the domain C (Fig. 16). However, the H-cells in the directions 47 deg and 49 deg, 53 deg experience the failure of bond 1 in compression first and then the failure of bond 2 in traction, which is consistent with the existence of domain B. The response of H-cells along the directions 55 deg and 71 deg is dominated by the failure of bond 2 in a traction regime, as observed in domain A.

The evolution of the meso-strains for the H-cells in the direction (53.5 deg) is shown in the Fig. 18. It can be seen that the mechanical behavior of the H-cells is in compression first, whatever the meso-strain (ε_n, ε_t). The meso-strain is derived from the macroscopic strain, and a sharp volume change is observed at the axial strain of 0.86%, due to the massive bond failure in traction. Thus, the meso-strain also experiences a sharp evolution, especially for the meso-strain ε_n with a transition from a compression regime to an extension regime, while the meso-strain ε_t is still in a compression regime. Fig. 19 shows the response of contact forces along a biaxial loading path. The normal contact forces (F_{n1}, F_{n2}) are in compression first, as observed for the meso-strains. At the axial strain of 0.86%, the meso-strain ε_n vanishes and takes negative values, indicating that an extension regime occurs. As a result, the normal contact force F_{n2} becomes a traction force. However, the normal contact force F_{n1} remains in compression, as the meso-strain ε_t still corresponds to a compression. In Fig. 19, the normal contact force F_{n1} reaches the compression strength limit, causing the failure of bond 1 in compression. The residual contact law is activated and the tangential contact force F_{t1} reaches the Mohr-Coulomb friction limit. Then, the H-cell meso-stress vanishes once the bond 2 brakes in traction.

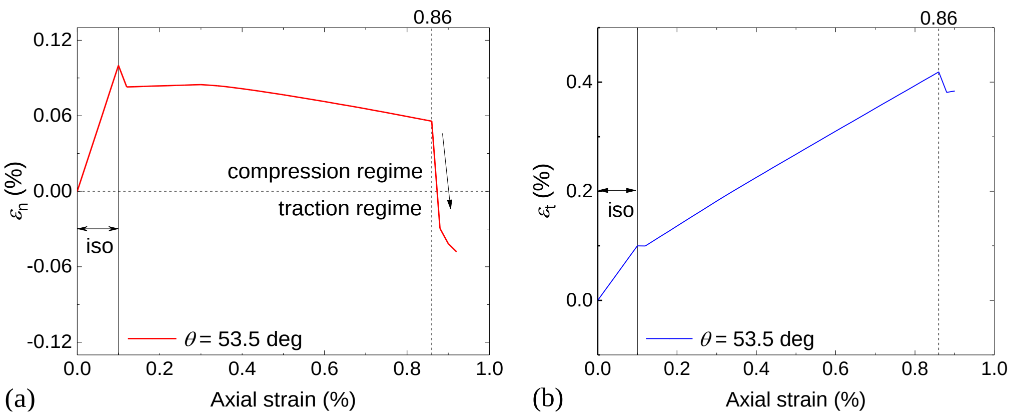

Fig. 18. Evolution of meso-strain components ε_n (relative length variation in the H-cell orientation) and ε_1 (relative length variation perpendicular to the H-cell orientation) for the H-cell in the direction $\theta = 53.5$ deg along a biaxial loading path.

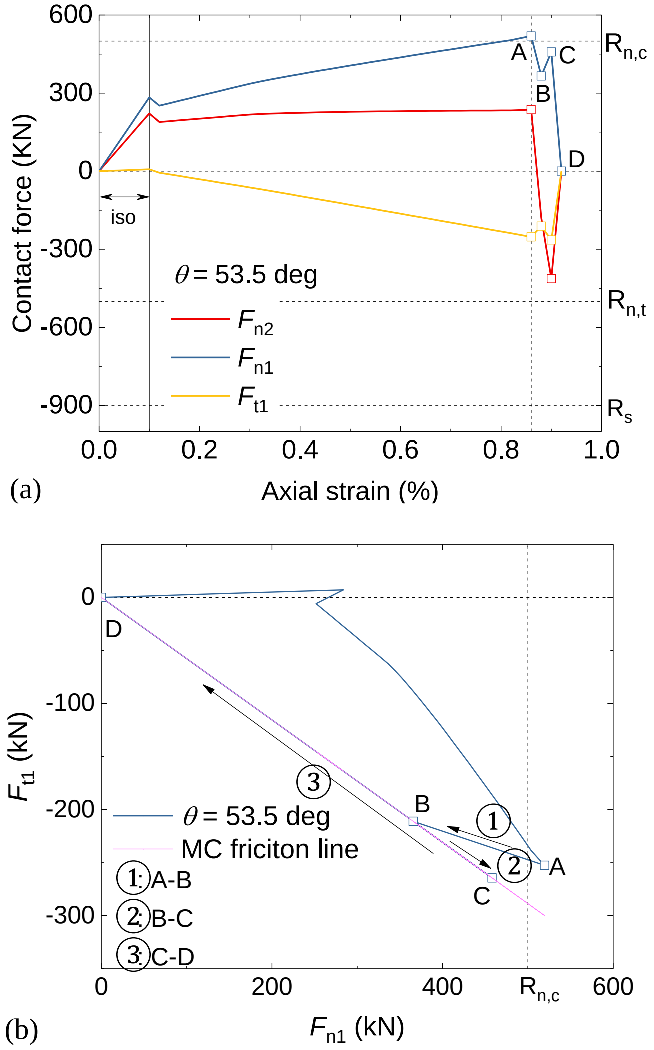

Fig. 19. Evolution of contact forces within the H-cell oriented in the direction $\theta = 53.5$ deg along a biaxial loading path (a); evolution of the contact force for bond 1 within the Mohr-Coulomb plane (b).

Figure 20 shows the mechanical behavior of the H-cells in the direction $\theta = 49$ deg. The H-cell is in contraction first along both axial and lateral directions. Then the meso-strain ε_n gradually decreases and reaches an extension regime. Fig. 21b shows that the normal contact force F_{n1} reaches first the compression strength limit, making bond 1 fail. Meanwhile, the normal contact force in bond 2 evolves from a compression regime to a traction regime until the bond fails.

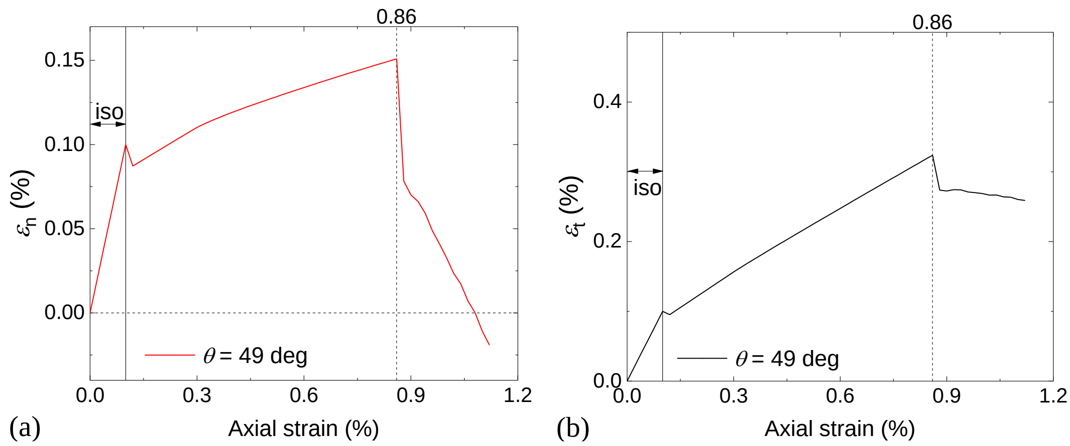

Fig. 20. Evolution of meso-strain components ε_n (relative length variation in the H-cell orientation) and ε_1 (relative length variation perpendicular to the H-cell orientation) for the H-cells in the direction $\theta = 49$ deg along a biaxial loading path.

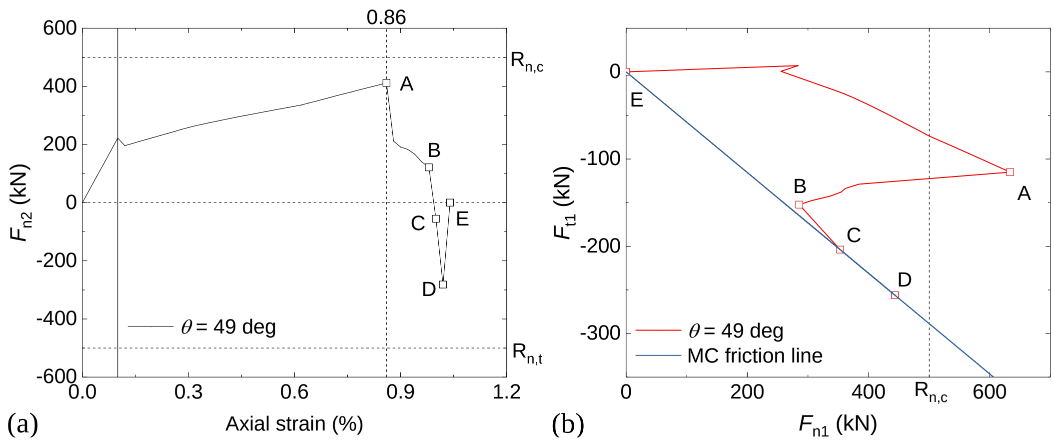

Fig. 21. Evolution of the contact force for bond 2 in the H-cell oriented in the direction $\theta = 49$ deg along a biaxial loading path (a); evolution of the contact force for bond 1 within the Mohr-Coulomb plane (b).

3.5 Limitations of the *H*-bond model

The *H*-bond model is an example of micromechanically-based model, departing from usual phenomenological models that require sophisticated formulations to capture the complexity observed on the macroscopic scale. Micromechanically-based models assume that the complexity stems mainly from the structural intricacy (geometrical complexity), whereas the local contact law between particles can be formulated in a very straightforward manner. In this perspective, the local constitutive relations taking place at contacts in the *H*-bond model are very simple, without any phenomenological sophistication, if at all possible. This simplicity can of course be debated in the specific case of the *H*-model, as the microstructural diversity cannot be approached as precisely as it can be done when using a Discrete Element Method. Indeed, the *H*-model assumes

that the granular assembly is simply described by a spatial distribution of independent hexagonal grain patterns. Each hexagon, oriented along a given direction of the physical space, contributes to the total stress existing within the assembly. However, the different hexagons do not interact with each other. It should also be noted that, compared with cohesionless granular materials, typical mesostructures found in (2D) cohesive granular materials can be larger than hexagons (cohesive bonds between particles contribute to a better mechanical stability of mesostructures containing larger numbers of grains), which results in longer correlation lengths within the assembly. It is clear that more complex criteria can be selected to describe bond failure. In this manuscript, it was assumed that the three failure modes (traction, compression and shear) are independent, disregarding more complex, coupled formulation including shear and traction/compression effects within a unique plastic limit surface. In addition, we have adopted the same strengths for all the bonds, which may result in more abrupt failure patterns (as observed in Figs. 13 and 14). This first approach was necessary to have a first overview of the model capability, before favoring a more complex, random distribution of strengths for the different bonds.
Furthermore, as the grains themselves constitute the microscopic (i.e. smallest) scale, we disregard any processes taking place at a smaller scale. Thus, the likely irregular shape of grains after bond failure cannot be captured by the model. This simplification is mainly debatable when dealing with cemented granular materials, where skeleton grains are immerged within a cemented matrix. If we restrict the current approach to granular assemblies with independent solid bonds between grains, this approximation is probably much more reasonable.
In spite of these inherent limitations, the approach stands as a first attempt to address the case of bonded granular assemblies, by developing a full micromechanically-based model. Even though the above-mentioned limitations should be carefully considered in future works, the results presented in this manuscript suggest that this approach can be deemed as a powerful alternative to standard phenomenological approaches.

4. Conclusion

In this paper, the behavior of cemented granular materials is investigated by considering the extended *H*-bond model and the underpinning microstructural mechanisms taking place within bonds. The model represents the granular assembly by a distribution of hexagonal patterns of contacting grains with solid bonds.

Each bond is described by a triad including two spherical particles linked by an intermediate beam-like bond, in which three failure modes (compression, traction, and shear) can occur. Once a bond has failed, it is supposed not to exist any longer, and the corresponding triad is replaced with a standard, unbonded pair of grains in elasto-frictional interaction.

By simulating biaxial loading paths and proportional strain loading paths, the interplay between the different bond failure modes has been explored. It is shown that the bond has an effect mostly in the early stage of loading, where a higher deviatoric stress peak occurs with a more pronounced, subsequent softening regime. As expected, the increasing bond strength contributes to an increase in this peak stress. Furthermore, depending on the bond strength in compression, tension and shear, the bonds are likely to break along preferential orientations. Progressively, the stress-strain response curve approaches the one that would have been obtained for a cohesionless specimen. These results are consistent with the conclusion drawn by Jiang et al. (2013).

When proportional strain loading paths are considered, it is shown that the bonds are also persistent at the beginning of the loading, whatever the volumetric strain regime (contractant, dilatant or isochoric). Likewise, depending on the bond strength in compression, tension and shear, the bonds fail in compression regime first, as the more loaded bonds are in a compressive regime at the beginning of the loading. Then, the contacts open when the tensile strength is reached.

More interestingly is the relation observed by tracking the process of bond failure during the loading paths. The evolution of both the bond failure ratio and the bond failure rate along the biaxial loading reveals that the peak of the bond failure rate coincides with the peak stress, and is followed by a sharp, subsequent decrease. As the bonds break in traction, the corresponding H-cells vanish, resulting in fewer cells involved in the macroscopic stress. Hence, a remarkable reduction in the macroscopic stress occurs, leading to a noticeable softening.

Analyzing the microscopic mechanical behavior offers more insight to understand the macroscopic response. Along biaxial loading paths, both bond 1 and bond 2 in a H-cell experience failure in a compression regime along the axial loading direction, while the bonds are gradually dominated by a traction or a shear regime, leading bonds to a tensile or shear failure in the lateral direction. For a particular range of directions, bond 1 first fails in a compression regime leading to the change in contact stiffness, which results in an earlier failure of bond 2 in traction.

Finally, the *H*-bond model is versatile and its micromechanical description makes it possible to investigate at the intermediate scale the origins of various macroscopic properties.

CRediT authorship contribution

Zeyong Liu: Investigation, Simulation, Validation, Methodology, Writing – original draft. **Francois Nicot:** Supervision, Conceptualization, Writing – review & editing. **Antoine Wautier:** Supervision, Methodology, Writing – review & editing. **Felix Darve:** Writing – review & editing.

Acknowledgments

The authors would like to warmly thank Doctor Chaofa Zhao (Zhejiang University), Professor Oliver Millet (La Rochelle University) and Doctor Yannick Thiery (BRGM) for the insightful discussions and constructive suggestions during this research work. The authors extend their sincere thanks for the support of the China Scholarship Council (CSC) and the BRGM (French Geological Service).

Appendix A

In the compression regime, once bond is broken, the triad reduces in a single contact between two particles. The normal contact force is described by an elastic relation, with a stiffness different from that prior failure (Fig. 22). Indeed, for a serial bond contact model, a triad (particle-bond-particle) is composed of three springs. Before bond failure, the normal contact force evolution is given by equation (1), with a stiffness reported in equation (3). Upon bond failure, the normal contact force evolution is given by equation (5), and the stiffness is reported in equation (7). It can be seen (Fig. 22) that after bond failure, a total unloading until zero normal force leads to a residual normal displacement $(u - u')$, where u' stands as the reversible part of the total normal displacement u.

The displacement u of the triad before bond failure is given by:

$$u = \frac{F_n}{k_n} \tag{A1}$$

whereas the reversible part u' of the displacement expresses as:

$$u' = \frac{F_n}{k_n'} \tag{A2}$$

The residual part $(u - u')$ is the consequence of the triad damage, associated with a change in the total stiffness (Grassl and Jirásek, 2006). By combining equations (A1) and (A2), it can be obtained:

$$u - u' = F_n\left(\frac{1}{k_n} - \frac{1}{k_n'}\right) \tag{A3}$$

Combining equations (3) and (7) expressed with the relationship involving the total stiffness and the stiffness of particles (k_{np}) and bond (k_{nb}) in a triad, yields the following equation (A4):

$$u - u' = \frac{F_n}{k_{nb}} \tag{A4}$$

where the residual normal displacement $(u - u')$ is expressed as a function of the normal stiffness of bond k_{nb}.

It should be noted that $u_b = u - u'$ corresponds to the elastic part of the normal displacement within the bond. After failure, this part of the displacement will not be recovered.

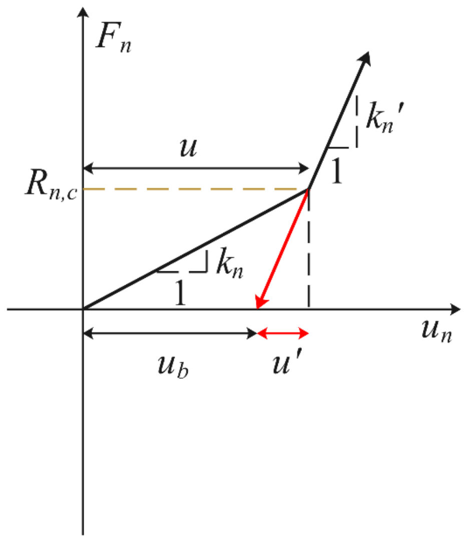

Fig. 22. Evolution of normal contact forces for a bonded contact, prior and after bond failure.

References

Abdulla, A.A., Kiousis, P.D., 1997. Behavior of cemented sands—II. Modelling. International Journal for Numerical and Analytical Methods in Geomechanics 21, 549–568.

Aboul Hosn, R., Sibille, L., Benahmed, N., Chareyre, B., 2016. Discrete numerical modeling of loose soil with spherical particles and interparticle rolling friction. Granular Matter 19, 4.

Balendran, B., Nemat-Nasser, S., 1993a. Double sliding model for cyclic deformation of granular materials, including dilatancy effects. Journal of the Mechanics and Physics of Solids 41, 573–612.

Balendran, B., Nemat-Nasser, S., 1993b. Viscoplastic flow of planar granular materials. Mechanics of Materials, Special Issue on Mechanics of Granular Materials 16, 1–12.

Brendel, L., Török, J., Kirsch, R., Bröckel, U., 2011. A contact model for the yielding of caked granular materials. Granular Matter 13, 777–786.

Burland, J.B., 1990. On the compressibility and shear strength of natural clays. Géotechnique 40, 329–378.

Consoli, N.C., Foppa, D., Festugato, L., Heineck, K.S., 2007. Key Parameters for Strength Control of Artificially Cemented Soils. J. Geotech. Geoenviron. Eng. 133, 197–205.

Coop, M.R., Atkinson, J.H., 1994. Discussion: The mechanics of cemented carbonate sands. Géotechnique 44, 533–537.

Cuccovillo, T., Coop, M.R., 1999. On the mechanics of structured sands. Géotechnique 49, 741–760.

Cuccovillo, T., Coop, M.R., 1997. Yielding and pre-failure deformation of structured sands. Géotechnique 47, 491–508.

Evans, T., Khoubani, A., Montoya, B., 2014. Simulating mechanical response in biocemented sands. https://doi.org/10.1201/b17435-277

Feng, K., Montoya, B.M., Evans, T.M., 2017. Discrete element method simulations of bio-cemented sands. Computers and Geotechnics 85, 139–150.

Gao, Z., Zhao, J., 2012. Constitutive modeling of artificially cemented sand by considering fabric anisotropy. Computers and Geotechnics 41, 57–69.

Giry, C., Dufour, F., Mazars, J., 2011. Stress-based nonlocal damage model. International Journal of Solids and Structures 48, 3431–3443.

Grassl, P., Jirásek, M., 2006. Damage-plastic model for concrete failure. International Journal of Solids and Structures 43, 7166–7196.

Huang, J.T., Airey, D.W., 1998. Properties of Artificially Cemented Carbonate Sand. J. Geotech. Geoenviron. Eng. 124, 492–499.

Ismail, M.A., Joer, H.A., Sim, W.H., Randolph, M.F., 2002. Effect of Cement Type on Shear Behavior of Cemented Calcareous Soil. J. Geotech. Geoenviron. Eng. 128, 520–529.

Jiang, M., Liu, F., Zhou, Y., 2014a. A bond failure criterion for DEM simulations of cemented geomaterials considering variable bond thickness. Int. J. Num. Anal. Meth. Geomech. 38, 1871–1897.

Jiang, M., Zhu, F., Liu, F., Utili, S., 2014b. A bond contact model for methane hydrate-bearing sediments with interparticle cementation. Int. J. Num. Anal. Meth. Geomech. 38, 1823–1854.

Jiang, M.J., Liu, J., Sun, Y., Yin, Z., 2013. Investigation into macroscopic and microscopic behaviors of bonded sands using distinct element method. Soils and Foundations 53, 804–819.

Kavvadas, M., Amorosi, A., 2000. A constitutive model for structured soils. Géotechnique 50, 263–273.

Khoubani, A., 2018. A New Bonding Model for the Particulate Simulation of Bio-Cemented Sand (with a Side Excursion on Percolation in Granular Mixtures).

Kochmanová, N., Tanaka, H., 2011. Influence of the Soil Fabric on the Mechanical Properties of Unsaturated Clays. Soils and Foundations 51, 275–286.

Lade, P.V., Overton, D.D., 1989. Cementation Effects in Frictional Materials. J. Geotech. Eng. 115, 1373–1387.

Leroueil, S., Vaughan, P.R., 1990. The general and congruent effects of structure in natural soils and weak rocks. Géotechnique 40, 467–488.

Li, Z., Wang, Y.H., Ma, C.H., Mok, C.M.B., 2017. Experimental characterization and 3D DEM simulation of bond breakages in artificially cemented sands with different bond strengths when subjected to triaxial shearing. Acta Geotech. 12, 987–1002.

Lin, H., Suleiman, M.T., Brown, D.G., Kavazanjian, E., 2016. Mechanical Behavior of Sands Treated by Microbially Induced Carbonate Precipitation. J. Geotech. Geoenviron. Eng. 142, 04015066.

Mazars, J., Pijaudier-Cabot, G., 1989. Continuum Damage Theory—Application to Concrete. J. Eng. Mech. 115, 345–365.

Mehrabadi, M.M., Loret, B., Nemat-Nasser, S., 1997. Incremental constitutive relations for granular materials based on micromechanics. Proceedings of the Royal Society of London. Series A: Mathematical and Physical Sciences 441, 433–463.

Montoya, B.M., DeJong, J.T., 2015. Stress-Strain Behavior of Sands Cemented by Microbially Induced Calcite Precipitation. J. Geotech. Geoenviron. Eng. 141, 04015019.

Nafisi, A., Safavizadeh, S., Montoya, B.M., 2019. Influence of Microbe and Enzyme-Induced Treatments on Cemented Sand Shear Response. J. Geotech. Geoenviron. Eng. 145, 06019008.

Nemat-Nasser, S., 2000. A micromechanically-based constitutive model for frictional deformation of granular materials. Journal of the Mechanics and Physics of Solids 48, 1541–1563.

Nemat-Nasser, S., Zhang, J., 2002. Constitutive relations for cohesionless frictional granular materials. International Journal of Plasticity 18, 531–547.

Nicot, F., Darve, F., 2011a. Diffuse and localized failure modes: Two competing mechanisms. Int. J. Num. Anal. Meth. Geomech. 35, 586–601.

Nicot, F., Darve, F., 2011b. The H-microdirectional model: Accounting for a mesoscopic scale. Mechanics of Materials 43, 918–929.

Nicot, F., Darve, F., 2005. A multi-scale approach to granular materials. Mechanics of Materials. 37 (9), 980–1006.

Obermayr, M., Dressler, K., Vrettos, C., Eberhard, P., 2013. A bonded-particle model for cemented sand. Computers and Geotechnics 49, 299–313.

Pettijohn, F.J., Potter, P.E., Siever, R., 1987. Sand and Sandstone. Springer, New York, NY. https://doi.org/10.1007/978-1-4612-1066-5

Rabbi, A.T.M.Z., Kuwano, J., Deng, J., Boon, T.W., 2011. Effect of Curing Stress and Period on the Mechanical Properties of Cement-Mixed Sand. Soils and Foundations 51, 651–661.

Rahman, Z.A., Toll, D.G., Gallipoli, D., Taha, M.R., 2010. Micro-structure and Engineering Behaviour of Weakly Bonded Soil. Sains Malaysiana 39, 989–997.

Rahman, Z.A., Toll, D. G., & Gallipoli, D., 2018. Critical state behaviour of weakly bonded soil in drained state. Geomechanics and Geoengineering, 13(4), 233-245.

Rios, S., Viana da Fonseca, A., Baudet, B.A., 2014. On the shearing behaviour of an artificially cemented soil. Acta Geotech. 9, 215–226.

Rocchi, G., Fontana, M., Da Prat, M., 2003. Modelling of natural soft clay destruction processes using viscoplasticity theory. Géotechnique 53, 729–745.

Rotta, G.V., Consoli, N.C., Prietto, P.D.M., Coop, M.R., Graham, J., 2003. Isotropic yielding in an artificially cemented soil cured under stress. Géotechnique 53, 493–501.

Rouainia, M., Muir wood, D., 2000. A kinematic hardening constitutive model for natural clays with loss of structure. Géotechnique 50, 153–164.

Shen, Z., Jiang, M., Thornton, C., 2016. DEM simulation of bonded granular material. Part I: Contact model and application to cemented sand. Computers and Geotechnics 75, 192–209.

Taheri, A., Sasaki, Y., Tatsuoka, F., Watanabe, K., 2012. Strength and deformation characteristics of cement-mixed gravelly soil in multiple-step triaxial compression. Soils and Foundations 52, 126–145.

Tang, C., Shi, B., Gao, W., Chen, F., Cai, Y., 2007. Strength and mechanical behavior of short polypropylene fiber reinforced and cement stabilized clayey soil. Geotextiles and Geomembranes 25, 194–202.

Terzis, D., Laloui, L., 2018. 3-D micro-architecture and mechanical response of soil cemented via microbial-induced calcite precipitation. Sci Rep 8, 1416.

Wang, Y.H., Leung, S.C., 2008. Characterization of Cemented Sand by Experimental and Numerical Investigations. J. Geotech. Geoenviron. Eng. 134, 992–1004.

Wautier, A., Veylon, G., Miot, M., Pouragha, M., Nicot, F., Wan, R., Darve, F., 2021. Multiscale modelling of granular materials in boundary value problems accounting for mesoscale mechanisms. Computers and Geotechnics 134, 104143.

Wu, M., Huang, R., Wang, J., 2021. DEM simulations of cemented sands with a statistical representation of micro-bond parameters. Powder Technology 379, 96–107.

Xiao, Y., Wang, Y., Wang, S., Evans, T.M., Stuedlein, A.W., Chu, J., Zhao, C., Wu, H., Liu, H., 2021. Homogeneity and mechanical behaviors of sands improved by a temperature-controlled one-phase MICP method. Acta Geotech. 16, 1417–1427.

Xiong, H., Nicot, F., Yin, Z.Y., 2017. A three-dimensional micromechanically based model. Num Anal Meth Geomechanics 41, 1669–1686.

Xiong, H., Yin, Z.-Y., Nicot, F., Wautier, A., Marie, M., Darve, F., Veylon, G., Philippe, P., 2021. A novel multi-scale large deformation approach for modelling of granular collapse. Acta Geotech. 16, 2371–2388.

Yang, P., Kavazanjian, E., Neithalath, N., 2019. Particle-Scale Mechanisms in Undrained Triaxial Compression of Biocemented Sands: Insights from 3D DEM Simulations with Flexible Boundary. Int. J. Geomech. 19, 04019009.

Yin, Z.-Y., Karstunen, M., 2011. Modelling strain-rate-dependency of natural soft clays combined with anisotropy and destructuration. Acta Mech. Solida Sin. 24, 216–230.

Zhang, A., Dieudonné, A.-C., 2023. Effects of carbonate distribution pattern on the mechanical behaviour of bio-cemented sands: A DEM study. Computers and Geotechnics 154, 105152.